Journal of the European Ceramic Society 40 (2020) 4428–4435

Contents lists available at ScienceDirect

Journal of the European Ceramic Society

journal homepage: www.elsevier.com/locate/jeurceramsoc

Original Article

# Enhanced strength and ductility of superhard boron carbide through injecting electrons

Yi He[a], Yidi Shen[b], Bin Tang[a,*], Qi An[b,*]

[a] State Key Laboratory of Electronic Thin Films and Integrated Devices, University of Electronic Science and Technology of China, Chengdu, 610054, China
[b] Department of Chemical and Materials Engineering, University of Nevada-Reno, Reno, Nevada, 89557, United States

ARTICLE INFO

*Keywords:*
$B_4C$
Failure
DFT
Mechanical properties
Injected carriers

ABSTRACT

Injected electrons and holes play an important role in the mechanical properties of semiconductors because of the charged states in dislocation core. However, many superhard ceramics exhibit very limited plasticity at room temperature because of strong covalent and ionic bonding. To illustrate the effects of injected carriers on the mechanical properties of superhard ceramics, we selected boron carbide ($B_4C$) as the prototype system and employed density functional theory (DFT) to examine the deformation and failure mechanism under neutral, injected-electron and injected-hole states. We find that both strength and ductility of $B_4C$ can be enhanced by injecting electrons, which arises from the modified failure mechanism due to the distribution of excess electrons. In contrast, injecting holes into $B_4C$ does not affect the failure mechanism, but causes increased strength and decreased ductility. Our study suggesting that injecting electrons is a promising way to tune mechanical properties of superhard ceramics.

## 1. Introduction

The superhard boron carbide is potentially used in many engineering applications such as refractories, coating and abrasive powders, anti-ballistic armor plating and high temperature semiconductor because of its unique physical properties of good thermal stability, excellent wear resistance, low density, and high hardness [1–3]. These promising mechanical and electronic properties arise from its unique crystal structure composed of 3-atom chains (C-B–C) and 12-atom icosahedral clusters ($B_{12}$/$B_{11}C$) [4], as well as the complex chemical bonding involving 26 electrons delocalized within $B_{12}$ icosahedron [1,5]. However, boron carbide suffers from the abnormal brittle failure above the critical failure strength because of the formation of amorphous shear bands which are measured to be 2 ~ 3 nm in width and 100 ~ 300 nm in length. The amorphous shear bands arise from deconstructing the ($B_{11}C$) icosahedral clusters in crystalline phase through the interaction of C-B–C chain with $B_{11}C$ icosahedron under shear deformation [6,7]. Therefore, it is essential to mitigate the amorphous shear band formation in $B_4C$ for its extended engineering applications. Many attempts have been made to improve the mechanical properties of boron carbide [8–12]. Previous experimental and theoretical studies demonstrated that microalloying Mg, Si and Li into boron carbide can improve its strength or mitigate the formation of amorphous shear bands [8,13–17]. Another approach is to introduce nanoscale twins in $B_4C$ that can enhance its theoretical strength, leading to a higher stress barrier of forming amorphous shear bands [10]. Moreover, grain boundary (GB) engineering with a higher energy GB phase leads to the GB sliding dominated deformation mechanism and enhanced ductility [18,19], suggesting that nanocrystalline boron carbide has superior mechanical properties to bulk $B_4C$ with micron size grains [18,19].

The structural failure of $B_4C$ is intrinsically related to its complex bonding and electronic structures. While it remains unknow how the electronic structures influent the failure mechanism of boron carbide. Boron carbide is a *p*-type semiconductor [1] and its bandgaps vary from 2.53 to 3.84 eV as the stoichiometry changes from ($B_{12}$)CCC to ($B_{11}C$)CBC [20]. Previous experiments indicated that electrons and holes play an essential role in the deformation and failure mechanism of semiconducting materials [21–23]. Particularly, the ionic semiconductor ZnS exhibits a ductile behavior at darkness while it suffers from brittle failure under light irradiation [24,25]. To explain this phenomenon, a recent study with constrained density functional theory (CDFT) simulations showed that the photo-induced electron-hole pairs significantly decrease the energy barriers of deformation slip, leading to a shift from dislocation nucleation under darkness to the twin dominated deformation under light irradiation condition [25]. In contrast, the same theoretical framework was applied to covalent semiconductor GaP and the results suggest an increased ductility under light-irradiation [26]. The theorical prediction was confirmed by the

---

* Corresponding author.
*E-mail addresses:* tangbin@uestc.edu.cn (B. Tang), qia@unr.edu (Q. An).

https://doi.org/10.1016/j.jeurceramsoc.2020.06.004
Received 15 April 2020; Received in revised form 30 May 2020; Accepted 2 June 2020

nanoindentation mechanical test and TEM experiments [27]. Furthermore, some recent studies indicated that injected electrons or holes also have a significant effect on the energy barrier of deformation slip, resulting in the different deformation mechanisms in semiconductors [28]. Therefore, it is expected that the mechanical properties of boron carbide could be modified under inject electron or hole states.

In the present work, we employed density functional theory (DFT) simulations at the Perdew-Burke-Ernzerhof (PBE) functional level [29] to examine how injected carriers influence the mechanical properties of boron carbide ($B_4C$) and boron rich boron carbide ($B_{13}C_2$). We first examined the effects of inject carriers on the elastic properties and found that elastic modulus of both $B_4C$ and $B_{13}C_2$ are changed with excess electrons or holes. Then the injected carriers were added into both $B_4C$ and $B_{13}C_2$ during the ideal shear deformation. We found that excess electrons enhance both strength and ductility of $B_4C$ due to the modification of failure mechanism. However, the excess holes improve the strength, yet decrease the ductility of $B_4C$ because of bond strengthening. In contrast to $B_4C$, the free carriers have limited effects on the deformation and mechanism process on $B_{13}C_2$. The physical origins of these simulation results are revealed through analyzing the chemical bonding and charge density difference between the charged states and the neutral state.

## 2. Computational methodology

All DFT simulations were carried out using periodic and plane-wave based code, VASP [30–32]. The core region of each atom is described using the pseudopotentials generated from projected augment wave (PAW) framework. The $2s^22p^1$ and $2s^22p^2$ electrons were treated as valence electrons for B and C, respectively. The exchange and correlation energy of electrons was computed using the generalized gradient approximation (GGA) type PBE functionals [29]. The number of plane waves used in all DFT simulations was determined by a cutoff value of 500 eV and the energy convergence for self-consistent field (SCF) iterations was set to $10^{-5}$ eV. The electron partial occupancy in each orbital was determined using the tetrahedron method with Blöchl correction [33]. The ions are allowed to move to minimum energy positions in geometry optimization using conjugate gradient method and the force convergence for the ion relaxation was $10^{-2}$ eV/Å. The integration over Brillouin zone is evaluated using the K-point sampling with the Monkhorst-Pack grid approach. The K-point meshes in all simulations were setup to a high resolution above $2\pi \times 1/40$ Å$^{-1}$.

We started from the experimental $B_{13}C_2$ rhombohedral crystal structure [34] and replaced one cage B atoms in the polar site with C atom to form $B_4C$. Then the lattice parameters and atomic positions of both $B_4C$ and $B_{13}C_2$ were optimized using DFT and the optimized structures were used for computing the elastic properties and deformation mechanism. Firstly, the elastic constant $C_{ij}$ was derived through the stress-strain relationship in the elastic regime when distorting the lattice by up to 0.3% along various directions [35,36]. Then, the stiffness constant $S_{ij}$, the inverse matrix of $C_{ij}$, is stemmed from $C_{ij}$ using $S_{ij} = (C_{ij})^{-1}$ [35,36]. Finally, the overall bulk modulus (K) and the shear modulus (G) of isotropic polycrystal could be derived from averaging Voigt bounds and Reuss bounds which are computed from $C_{ij}$ and $S_{ij}$, respectively [35,36].

To determine the atomistic deformation and failure mechanism of both $B_4C$ and $B_{13}C_2$, we performed ideal shear deformation along the most plausible slip system (001)[100] [7,9]. In the Article we adopted the 3-index rhombohedral slip system rather than 4-index hexagonal system. The ideal shear deformation is achieved by continuously shearing the system with the shear strain constrained along this slip direction while relaxing the cell parameters along other five strain components [37]. The residual stresses along the relaxed directions were less than 0.2 GPa. A 2 × 2 x 2 supercell with 120 atoms was used in the ideal shear deformation and a (3 × 3 x 3) K-point grid mesh in the Brillouin zone was employed.

In order to mimic the carrier-charged electron or hole states, we added or removed electrons from the constructed neutral systems, respectively. A homogeneous background-charge is automatically added to offset the unbalanced charge in the charged systems. The carrier concentrations are $\sim 1.1 \times 10^{21}$ cm$^{-3}$ in all electron-charged or hole-charged simulations. This high carrier concentration is comparable to the highly doped semiconductors [21–23]. To ascertain the chemical bonding information such as bonding nature and strength in solid-state, we applied Crystal Orbital Hamilton Population (COHP) [38] analyses implemented in LOBSTER package [38,39]. The COHP refers to a partitioning of the band structure energy into orbital-pair contributions. In the framework of COHP, bonding, anti-bonding and non-bonding are represented by negative, positive and zero values, respectively. The COHP was originally proposed for the local basis set and it can be projected into the plane-wave basis set to form projected COHP (pCOHP). The integrated pCOHP (IpCOHP) could be used to determine the bond strength, which is integrated from the starting band energy to the highest occupied state (Fermi energy). The higher value of IpCOHP corresponds to a stronger bond [40]. In addition, the charge density difference between the charged state and the neutral states was derived to illustrate the charge redistribution under electron (or hole) injected states. The electron localization function (ELF) analysis was performed to determine whether the bond breaks or not during shear deformation. The VESTA [41] software was used to visualize crystal structure, ELF and charge density difference.

## 3. Results and discussion

### 3.1. Modified crystal structure and elastic properties under charged states

The $B_4C$ belongs to the rhombohedral space group (R $\bar{3}$ m) and contains one icosahedral cage ($B_{12}/B_{11}C$) and one chain (C-B–C/CCC−−) in the rhombohedral unit cell [1]. The distribution of C atoms in the cage or chain influences the crystal symmetry. Previous DFT simulations revealed that the most plausible crystal structure is ($B_{11}C_p$)CBC in which the C is located in the cage and connects to the nearby icosahedron (polar site, denotated as subscript p) [1]. The less stable structure is ($B_{11}C_e$)CBC in which the cage carbon is connected to the C-B–C chain (equatorial sites, denotated as subscript e), and the most unstable structure is ($B_{12}$)CCC. This picture of $B_4C$ is consistent with very recent study comparing the computed X-ray powder diffraction (XRD) of various configurations with experimental measurement [42]. In the present study we focus on the most stable structure ($B_{11}C_p$)CBC and use it to represent the $B_4C$ although the experimental $B_4C$ sample may be a mixture of various possible configurations. The formula of ($B_{11}C_p$)CBC can be written as $(B_{11}C_p)^{1-}$[C-$B^+$-C] in which one electron from C-B–C chain transfers to the ($B_{11}C_p$) cage leading to 26 skeleton bonding electrons in the cage and satisfying Wade's rule [43,44]. The DFT optimized lattice parameters for ($B_{11}C_p$)CBC are a = 5.208 Å, b = 5.057 Å, c = 5.208 Å, α = 66.02°, β = 65.14°, and γ = 66.02°. After the 1/8 injected electrons was added to this unit cell, leading to a carrier concentration of $1.1 \times 10^{21}$ cm$^{-3}$, the lattice parameters change to a = 5.224 Å, b = 5.071 Å, c = 5.224 Å, α = 65.96°, β = 65.03°, and γ = 65.96°, indicating a volume increase. In contrast, the lattice parameters were decreased to a = 5.189 Å, b = 5.048 Å, c = 5.189 Å, α = 66.11°, β = 65.28°, and γ = 66.11° as 1/8 holes was injected into the neutral system.

Boron carbide has a wide range of solubility and the C content various from 8 to 20 at% [1]. As the C content decreases to 13.3 at%, it forms the composition of B-rich boron carbide (nominally $B_{13}C_2$). The $B_{13}C_2$ can be described as ($B_{12}$)CBC in which the cage C in $B_4C$ is replaced by B atom. It is challenging to describe the bonding of $B_{13}C_2$ using Wade's rule since two extra electrons are required for $B_{12}$ icosahedron while only one electron is available from C-B–C chain. The DFT optimized lattice constant for $B_{13}C_2$ are a = b = c = 5.196 Å, and α = β = γ = 65.95°. The injected electrons (1/8e to the unit cell) also leads

**Table 1**
The elastic modulus (K and G) of neutral, electron-injected, and hole-injected $B_4C$ and $B_{13}C_2$ (unit: GPa).

| | $K_V$ | $G_V$ | $K_R$ | $G_R$ | K | G | K/G |
|---|---|---|---|---|---|---|---|
| $B_4C$ | 238.83 | 202.93 | 237.19 | 194.70 | 238.01 | 198.82 | 1.197 |
| $B_4C+0.125e$ | 235.30 | 195.36 | 233.56 | 186.66 | 234.43 | 191.01 | 1.227 |
| $B_4C+0.125hole$ | 241.03 | 201.32 | 239.44 | 193.05 | 240.24 | 197.19 | 1.218 |
| $B_{13}C_2$ | 222.66 | 168.25 | 220.66 | 155.87 | 221.66 | 162.06 | 1.368 |
| $B_{13}C_2+0.125e$ | 219.97 | 169.35 | 218.15 | 157.13 | 219.06 | 163.24 | 1.342 |
| $B_{13}C_2+0.125hole$ | 225.58 | 165.25 | 223.38 | 151.59 | 224.48 | 158.42 | 1.417 |

to the expansion of unit cell with the lattice parameters of a = 5.212 Å and α = 65.84° and the injected holes (1/8 h) resulting in the shrink of lattice parameter (a = 5.180 Å and α = 66.07°).

The injected electrons and holes are expected to influence the elastic properties of boron carbide. To illustrate this effect, we used Voigt-Ruess-Hill approximation to compute the bulk modulus (K) and shear modulus (G) of neutral, electron-injected and hole-injected systems. Furthermore, the K/G is computed as the indicator of the brittleness based on Pugh's criterion [45]. The computed K, G and K/G are listed in Table 1. For 1/8 electrons injected $B_4C$, the K and G decrease by 1.50% and 3.93% compared to neutral $B_4C$, respectively, indicating that excess electrons weaken the $B_4C$. However, the K/G is increased by 2.51% than that of neutral $B_4C$, suggesting that the ductility is slightly enhanced. In contrast, the K increases by 0.94% but the G decreases by 0.82% compared to neutral $B_4C$ as 1/8 holes are added. This also leads to an increase of B/G by 1.75% and the enhanced ductility with excess holes.

As the excess electrons are added to $B_{13}C_2$, the modified elastic properties exhibit different behaviors compared to $B_4C$. As shown in Table 1, adding 1/8 excess electrons into $B_{13}C_2$ leads to a decrease of K by 1.17%, but an increase of G by 0.73%. Therefore, the K/G and ductility of $B_{13}C_2$ decreases as extra electrons are added. In contrast, as 1/8 holes are added, the K increases by 1.27% and G decreases by 2.25%, which is the same trend as injected electrons. The K/G increases by 3.80%, indicating a higher ductility. Therefore, electron charged state leads to the decreased ductility while hole charged state increases ductility.

### *3.2. Modified deformation and failure mechanism of $B_4C$ under electron charged states*

To illustrate how excess electrons influence the intrinsic failure mechanism of $B_4C$, we performed the ideal shear deformation on electron-injected $B_4C$ and compared to the neutral system. To examine the carrier concentration effects, we added one electron to a 2 × 2 x 2 supercell, leading to a concentration of $1.14 \times 10^{21}$ $cm^{-3}$. It is important to check the energy and stress convergence of the charged images after the electrons are added to the neutral system. Thus, we constructed a 4 × 2 × 2 supercell and added two electrons, leading to the same concentration of $1.14 \times 10^{21}$ $cm^{-3}$. The shear-stress-shear-strain relationship of both systems, displayed in Fig. S1 of Supplementary Materials (SM), are overlapped before the failure, suggesting that it is reliable to use a 2 × 2 x 2 supercell to mimic the carrier concentration of $1.14 \times 10^{21}$ $cm^{-3}$. In addition, to illustrate the electron concentration effect, two electrons were added to the same supercell, leading to a double carrier concentration of $2.28 \times 10^{21}$ $cm^{-3}$.

Fig. 1 displays the shear-stress-shear-strain relationship of $B_4C$ along the (001)[100] slip system under neutral, 1e-injected and 2e-injected states. As the shear strain is less than 0.2, $B_4C$ deforms elastically under all states. The slope of the stress-strain curves is lower for the electron-charged states compared to the neutral state, suggesting that excess electrons weaken the $B_4C$. This is consistent with the effects on elastic modulus in which the shear modulus decreases as excess electrons are added. The shear stress reaches the first maximum and starts to decrease at ~0.2 strain because of the bond broken between icosahedra (discussed in detail later). The excess electrons decrease the first maximum shear stress and the higher carrier concertation leads to a more significant decrease. This process does not lead to the failure of $B_4C$ and the shear stress starts to increase at ~0.26 shear strain. After the shear stress reaches the second maximum value (ideal shear stress), the structure fails. It is interesting to notice that the extra electrons delay the failure process and increase the critical failure strain from 0.364 to 0.381. Meanwhile the ideal shear stress increases from 42.43 GPa at neutral state to 43.16 GPa and 42.99 GPa for 1e-injected and 2e-injected states, respectively. Therefore, adding excess electrons into $B_4C$ enhances both the strength and the ductility.

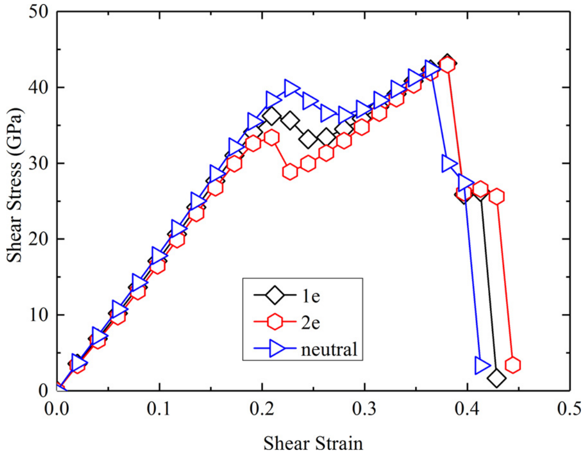

**Fig. 1.** The shear-stress-shear-strain curve of $B_4C$ along (001)[100] slip system under neutral, 1e-injected state and 2e-injected state, respectively.

The shear deformation of $B_4C$ along various plausible slip systems was investigated by previous DFT studies [7] and the (001)[100] slip system was identified as the most plausible slip system, which agrees well with nanoindentation experiments [46]. Then the failure mechanism of $B_4C$ along (001)[100] slip system was determined as follows. Firstly, the shear causes the icosahedral B–C bond broken between neighboring icosahedra, leading to the formation of carbene lone pair. Then the continuous shear makes the middle boron in the C-B–C chain reacts with carbene, stretching the icosahedra and deconstruing them, leading to the failure [7].

To illustrate how the excess electrons influence this failure process, we plotted the key structural changes for the shear deformation along (001)[100] slip system under 1e-injected state (Fig. 2). The intact structure is displayed in Fig. 2a. As the shear strain increases to 0.227, the structure undergoes elastic deformation and no bond breaks, as shown in Fig. 2b. The inter-icosahedral C8-B51 bond is continuously stretched under shear deformation, but the ELF analysis shows that this bond remains connected. When the shear strain increases to 0.245, this C8-B51 bond is fully broken and it is stretched to 2.650 Å (Fig. 2c). The ELF analysis shows that the electron lone pair moves entirely to the icosahedral C8, forming a carbene. No icosahedra are disintegrated, indicating that the structure is not failed. As the shear strain further increases to 0.381 corresponding to the maximum shear stress of 43.16 GPa (Fig. 2d), the icosahedra continuously slip to each other without deconstruction. Finally, the icosahedra are deconstructed because of the bond formation between cage B (B51) and the middle chain B (B92), as shown in Fig. 2e. This initiates the structure failure, releasing the accumulated shear stress. It is worth noting that the failure mechanism is different from the neutral system in which the structure failure starts from the middle B in the C-B–C chain reacting with the carbene C8, as shown in Fig. S2 of SM. The failure process of 2e-injected 4 × 2 × 2 supercell shear along (001)[100] slip system exhibits the same character, as shown in Fig. S1 of SM.

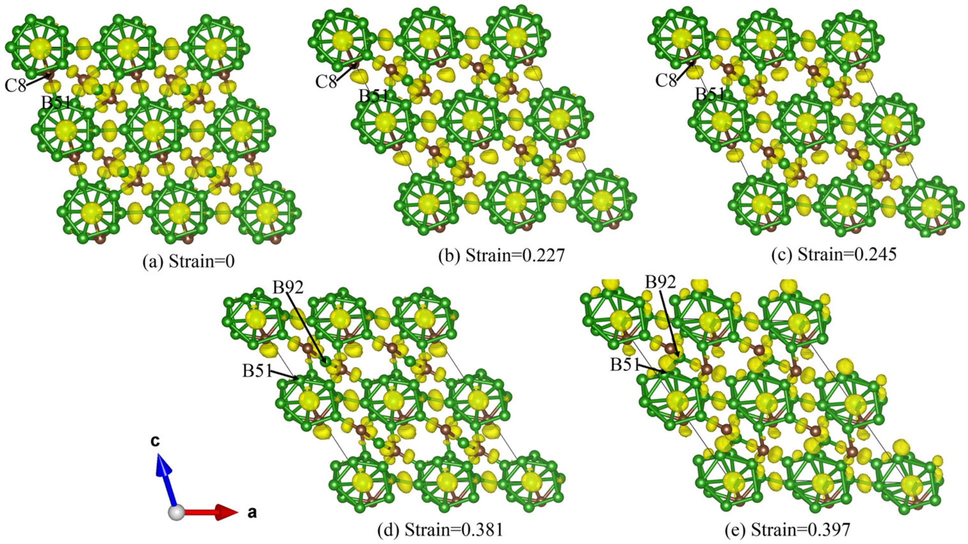

(a) Strain=0 (b) Strain=0.227 (c) Strain=0.245 (d) Strain=0.381 (e) Strain=0.397

**Fig. 2.** The structural evolution of 1e-injected $B_4C$ system shear along (001)[100] slip system: (a) The intact structure; (b) Structure at 0.227 shear strain before which the system undergoes elastic deformation; (c) Structure at 0.245 shear strain in which the C8-B51 bond breaks; (d) Structure at 0.381 shear strain corresponding to the ideal shear stress; (e) Failed structure at 0.397 shear strain in which failure arises from the interaction between cage B51 and chain B92. The B and C atoms are represented by green and sienna balls, respectively. The yellow isosurface represents the ELF analysis (ELF = 0.85).

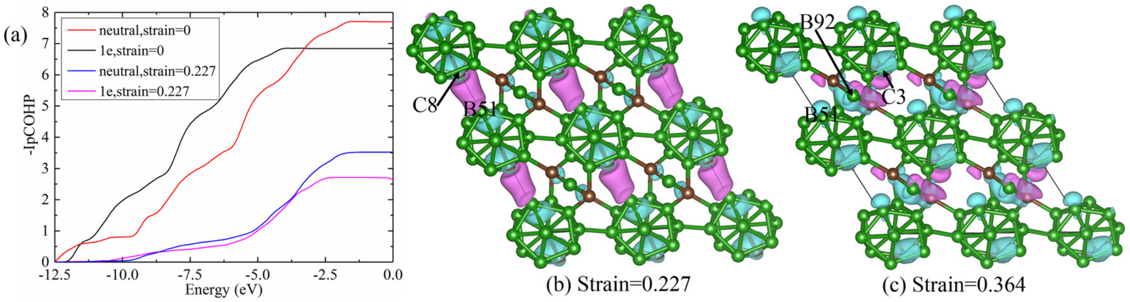

(b) Strain=0.227 (c) Strain=0.364

**Fig. 3.** (a) The IpCOHP for the icosahedral C8-B51 bond under the 1e-injected and the neutral states. (b) The charge density difference between the 1e-injected state and the neutral state at 0.227 shear strain. (c) The charge density difference between the 1e-injected state and the neutral state at 0.381 shear strain. The light blue and lavender isosurfaces represent the positive and the negative values, respectively.

To illustrate why extra electrons change the deformation mechanism of $B_4C$, we performed the quantum mechanical bonding indicator projected COHP (pCOHP) analysis. Firstly, the inter-icosahedral C8-B51 bond was analyzed since it is the initial bond broken under shear deformation. The pCOHP analyses for the icosahedral B–C bond under both neutral and 1e-injected states are shown in Fig. S3 of SM. Then we integrated the pCOHP to examine the change of bond strength after adding electrons. As shown in Fig. 3a, the value of integrated pCOHP (IpCOHP) is lower under 1e-injected state than that under neutral state, suggesting that the bond strength decreases with excess electrons. This decrease in bond strength can be observed from the analyses of both the intact structure (0.0 shear strain) and the deformed structure (0.227 shear strain). The bond strength decrease can be explained from the charge density difference between the 1e-injected state and the neutral state at 0.227 shear strain. As shown in Fig. 3b, the electrons are less distributed among the icosahedral B–C bond, while more distributed in the cage. This destabilizes the icosahedral B–C bond under 1e-injected state, which is consistent with the IpCOHP analysis. The weakened icosahedral B–C bond explains the decreased critical shear stress for the icosahedral B–C bond broken process.

To explain the modified failure mechanism of $B_4C$ under 1e-injected state, we further computed the charge density difference at 0.381 shear strain just before the deconstruction of icosahedra. As shown in Fig. 3c, the electrons are less distributed among chain B, carbene and chain C for the 1e-injected state compared to the neutral state. Particularly, there are missing electrons between chain B (B92) and carbene (C3), decreasing the electrostatic attraction between them and preventing their further bonding. However, there are some excess electrons distributed between B51 and B92, increasing their electrostatic attraction. Therefore, the B51 and B92 are bonded under 1e-injected state, leading to a different failure mechanism compared to the neutral system. At 0.364 shear strain, the bond distances of B51-B92 and C3-B92 are 2.987 Å and 2.786 Å for the 1e-injected state, respectively. While they are 3.018 Å and 2.723 Å under the neutral state, respectively. This suggests the increased interaction between B51-B92 and the decreased interaction between C3-B92 under the 1e-injected state, which is consistent with the analysis from charge density difference.

To examine the effect of carrier concentration, we added two electrons into the 2 × 2 x 2 supercell, leading to a carrier concentration of $2.28 \times 10^{21}$ cm$^{-3}$. The deformation mechanism remains the same as the 1e-injected state while more excess electrons weaken the system more, as shown in Fig. 1. The key structural changes for (001)[100] slip system under the 2e-injected state are displayed in Fig. 4. The intact structure is shown in Fig. 4a and the structure deforms elastically to 0.209 shear strain (Fig. 4b). Then the inter-icosahedral C8-B51 bond breaks at 0.227 shear strain with the bond distance stretched from 2.207 Å to 2.609 Å. It is worth noting that the critical strain for the icosahedral bond broken is less than that in the 1e-injected state and the neutral state. This suggests that more excess electrons further weaken this bond and make it easier to break. However, the icosahedra remain not deconstructed when the shear strain increases to 0.381 (Fig. 4d). Finally, the middle chain B (B92) is bonded to cage B (B51), leading to the disintegration of ($B_{11}C$) icosahedra and structural failure (Fig. 4e). This failure mechanism is the same as the 1e-injected state.

The carrier concentration in this study is high and close to the high doped semiconductors. It was expected that lower the carrier concentration decreases the effects of excess electrons. The deformation mechanism of lower electron concentration is expected to be similar to

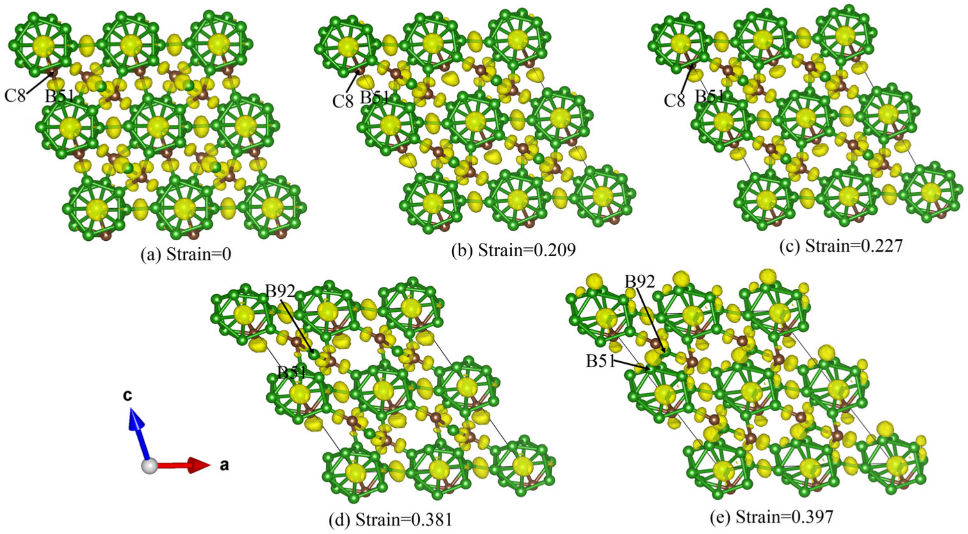

(a) Strain=0 (b) Strain=0.209 (c) Strain=0.227 (d) Strain=0.381 (e) Strain=0.397

**Fig. 4.** The structural evolution of 2e-injected $B_4C$ system along (001)[100] slip system: (a) The intact structure; (b) Structure at 0.209 shear strain until which the system undergoes elastic deformation; (c) Structure at 0.227 shear strain in which the inter-icosahedral B–C bond is broken; (d) Structure at 0.381 shear strain corresponding to the ideal shear stress; (e) Failed structure at 0.397 shear strain. The B and C atoms are represented by green and sienna balls, respectively. The ELF at various structures is represented by the yellow isosurface and the value of isosurface is 0.85.

the 1e-injected state at a relative high carrier concentration. However, as the carrier concentration is below some critical value, we expect that the mechanical behavior of $B_4C$ may be closer to the neutral system.

### 3.3. *Deformation and failure mechanism of $B_4C$ under hole charged states*

To illustrate how injected holes influence the intrinsic failure mechanism of $B_4C$, we performed the ideal shear deformation on the system in which one hole (1 h) is injected into a 2 × 2 x 2 supercell. The carrier concentration for 1 h-injected system is $1.16 \times 10^{21}$ cm$^{-3}$. The size effect on the charge states was examined by injecting two holes into a 4 × 2 × 2 supercell, leading to the same carrier concentration. The shear-stress-shear-strain relationships of both systems are displayed in Fig. S4 of SM and they are overlapped with each other, suggesting the reliability of using the 2 × 2 x 2 supercell. Furthermore, the effect of carrier concentration was illustrated by injecting two holes into the 2 × 2 x 2 supercell, leading to a hole concentration of $2.32 \times 10^{21}$ cm$^{-3}$.

Fig. 5 displays the shear-stress-shear-strain relationships of $B_4C$ shearing along (001)[100] slip system under neutral, 1 h-injected and 2 h-injected states. The slope of the stress-strain curves is almost identical for these states before 0.08 shear strain and then it decreases for the hole-charged states, indicating that excess holes weaken the $B_4C$. However, the excess holes increase the critical shear strain corresponding to the first stress drop, resulting in the increased critical shear stress. The higher carrier concentration even leads to a more significant increase on both the first critical shear stress and the critical shear strain. As discussed below, no icosahedra are deconstructed after the first critical shear strain. Instead, the structure fails after the shear stress passes the second maximum value. The extra holes decrease this critical failure stress and failure strain. As holes are injected, the ideal shear stress is switched from the 2$^{nd}$ critical failure stress to the first one. Therefore, the ideal shear stress increases from 42.43 GPa at the neutral state to 42.53 GPa and 43.09 GPa for 1 h-injected state and 2 h-injected state, respectively. Therefore, the strength of $B_4C$ increases, yet the ductility decreases after adding excess holes.

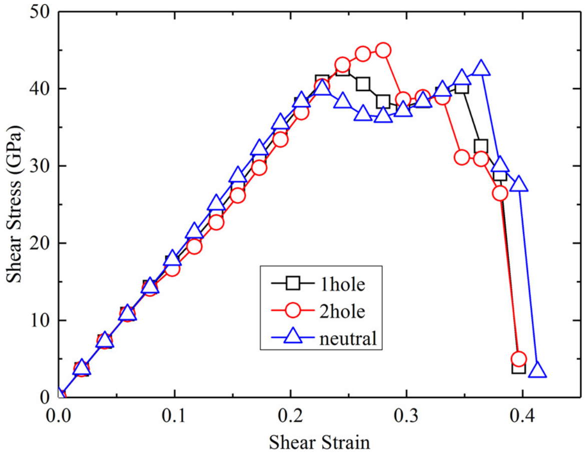

**Fig. 5.** The shear-stress-shear-strain relationships of $B_4C$ along (001)[100] slip system under neutral, 1 h-injected and 2 h-injected states, respectively.

To assess the structural evolution of 1 h-injected $B_4C$ under ideal shear deformation, we plotted the structures at several important strains along (001)[100] slip system, as shown in Fig. 6. The intact structure is displayed in Fig. 6a and it is deformed elastically until the shear strain increases to 0.245 that corresponds to the idea shear stress of 42.45 GPa (Fig. 6b). The inter-icosahedral C8-B51 bond is stretched from 1.654 Å to 2.173 Å at 0.245 shear strain but the ELF analysis shows that it is not broken. As the shear strain increases to 0.280, the inter-icosahedral C8-B51 bond is broken (Fig. 6c) with the distance significantly increased to 2.745 Å. The ELF analysis shows the formation of carbene lone pair after breaking the inter-icosahedral B–C bond. The icosahedra are not deconstructed as the shear strain increases to 0.348 (Fig. 6d). As the shear strain increases to 0.364 (Fig. 6e), the $B_{11}C$ icosahedra are deconstructed due to induced stretching as the middle chain B (B95) is bonded to the cage C (C8) and the bond distance decreases from 2.692 Å to 1.771 Å. This failure mechanism is different from 1e-injected state as discussed in Section 3.2, but it is the same as the neutral state. Injecting 2 h into a 4 × 2 × 2 supercell leads to the same carrier concentration and the shear deformation of this system exhibits the same structural changes, as shown in Fig. S4 of SM.

The IpCOHP analysis was performed to explain the 1 h-injected effects on $B_4C$. The IpCOHP was derived from pCOHP shown in Fig. S5 of SM. The IpCOHP of C8-B51 bond in both intact structure and deformed structure (0.227 shear strain), displayed Fig. 7a, shows that their values are larger under 1 h-injected state than those under the neutral state, indicating that the bond strength increases under the 1 h-injected state. Under 1 h-injected state, the deformed structure has a more promising bond strengthening than the intact structure, as indicated by a larger difference of IpCOHP value at Fermi energy for the deformed structure. The increase bond strength is also illustrated in the charge density difference between the 1 h-injected state and the neutral state, as shown in Fig. 7b. At 0.227 shear strain, there are less holes (or more electrons) distributed among the inter-icosahedral B–C bond under the 1 h-injected state, making it stronger than that under the neutral state. This explains that the B–C bond breaks at a larger shear

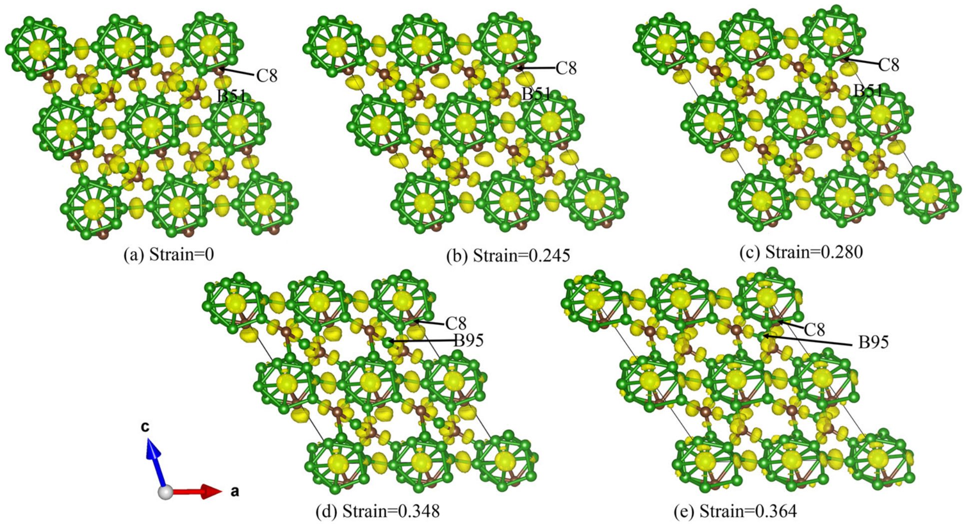

**Fig. 6.** The structural evolution of 1 h-injected $B_4C$ system along (001)[100] slip system: (a) The intact structure; (b) Structure at 0.245 shear strain corresponding to the maximum shear stress; (c) Structure at 0.280 shear strain in which the inter-icosahedral B–C bond is broken; (d) Structure at 0.348 shear strain before failure; (e) Failed structure at 0.364 shear strain. The B and C atoms are represented by green and sienna balls, respectively. The ELF is represented by yellow isosurface with a value of 0.85.

strain under the 1 h-injected state.

The deformation and failure mechanism of $B_4C$ under the 2 h-injected state is similar to the 1 h-injected state, as shown in Fig. S6 and discussed in SM. The higher hole concentration leads to a higher ideal shear stress and a lower failure strain, suggesting that adding more holes is benefit for the strength, yet deteriorate to the ductility. In contrast, we expect that lower hole concentration would lead to a lower ideal shear stress and a higher failure strain.

### 3.4. Modified deformation and failure mechanism $B_{13}C_2$ under charged state

To illustrate how injected carriers affect the intrinsic failure mechanism of $B_{13}C_2$, we performed the ideal shear deformation on 1e-injected $B_{13}C_2$ and one 1 h-injected $B_{13}C_2$ along (001)[100] slip system. The carrier concentrations are $\sim 1.1 \times 10^{21}$ $\mathrm{cm}^{-3}$ for both systems. The shear-stress-shear-strain relationships for the neutral, the 1e-injected and 1 h-injected states are shown in Fig. 8. The ideal shear stress of neutral, one electron injected and one hole injected states for (001)[100] slip system are 47.94 GPa, 47.96 GPa and 47.77 GPa, respectively, suggesting that electrons and holes have no significant effects on the shear deformation of $B_{13}C_2$.

To understand the structural evolution of $B_{13}C_2$ along (001)[100] slip system under 1e-injected state, three structures at critical strains are displayed in Fig. 9. The intact structure is shown in Fig. 9a. The system deforms elastically until the shear strain increases to the critical value of 0.348, that corresponds to the ideal shear stress of 47.96 GPa (Fig. 9b). As the shear strain further increases to 0.364 (Fig. 9c), the icosahedra are deconstructed due to the intra-icosahedral B21-B80 and B28-B65 bond stretching from 2.257 Å to 2.793 Å, leading to the structural failure. The failure mechanism is consistent with the neutral state, as discussed in previous study [9]. The deformation and failure mechanism of the 1 h-injected state is the same as the 1 h-injected state, as discussed in SM and Fig. S7.

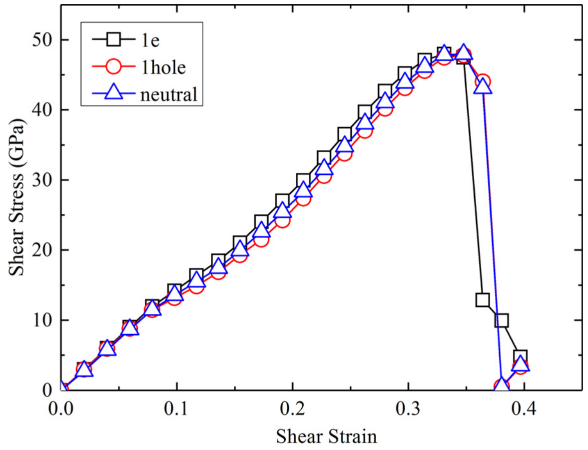

**Fig. 8.** The shear-stress-shear-strain curve of $B_{13}C_2$ along (001)[100] slip system under the 1e-injected, the 1 h-injected and the neutral states, respectively.

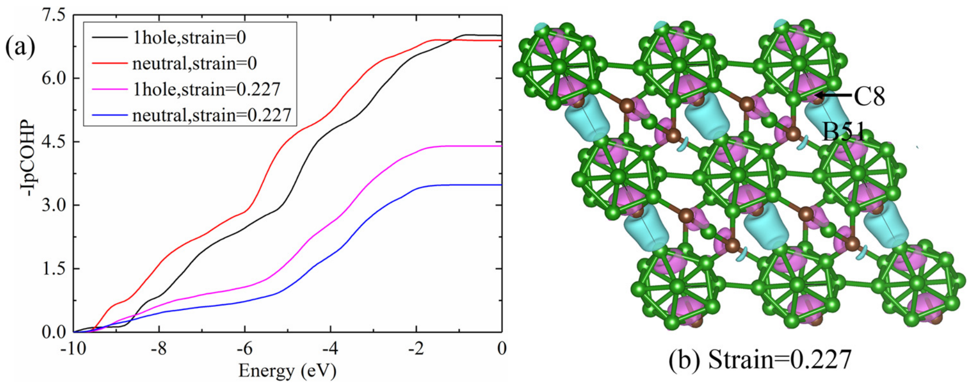

**Fig. 7.** (a) The integrated pCOHP for B–C bond under neutral and 1 h-injected states; (b) The charge density difference between 1 h-injected and neutral state at 0.227 shear strain. The light blue and lavender isosurfaces represent positive and negative values, respectively.

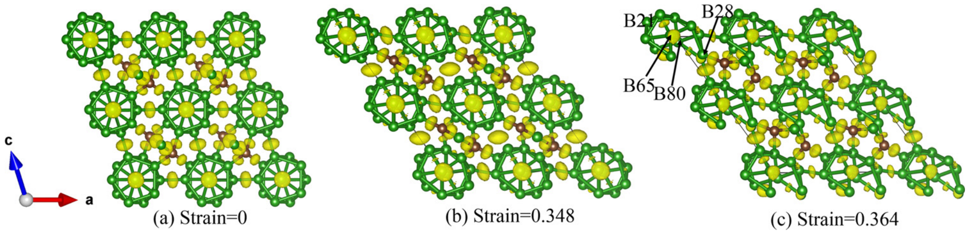

(a) Strain=0 (b) Strain=0.348 (c) Strain=0.364

**Fig. 9.** The structural evolution of 1e-injected $B_{13}C_2$ system shear along (001)[100] slip system: (a) The intact structure; (b) Structure at 0.348 shear strain that corresponds to the ideal shear strength; (c) Failed structure at 0.364 shear strain. The B and C atoms are represented by green and sienna balls, respectively. The ELF at various strains are represented by yellow isosurface with the value of 0.85.

## 4. Conclusion

In summary, the DFT simulations were performed to investigate the effects of injected carriers on the mechanical properties of boron carbide. The simulations results indicate that injected electrons lead to decreased K and G of $B_4C$, while to decreased K and increased G for $B_{13}C_2$. In contrast, the injected holes lead to increased K, yet decreased G for both $B_4C$ and $B_{13}C_2$. The deformation and failure mechanism of $B_4C$ are affected significantly by excess electrons and holes. Although the excess electrons weaken the bonding in $B_4C$, they improve both strength and ductility of $B_4C$ by modifying the failure mechanism from the interaction between chain B and cage C to the interaction between chain B and cage B. This arises from the less electrons distributed between chain B and cage C, as well as more electrons accumulated between chain B and cage B. This leads to the increased failure strain and higher critical stress under injected electron state. In contrast, the excess holes strengthen the bonding in $B_4C$ and increase the strength while it decreases the ductility by lowering the critical failure strain. For $B_{13}C_2$, no significant affects from free carriers were observed in our simulations since the deformation mechanism is the same as the neutral state. The present study suggests that injecting electrons into $B_4C$ is a promising way to design the superhard $B_4C$ with significant enhanced strength and ductility. The injected electrons may be achieved through doping elements with excess electrons.

Free electrons and holes may influence other materials behaviors, such as phase transition, plastic deformation, etc. The theoretical framework in this study could be applied to illustrate how electrons and holes influence these materials behaviors. Indeed, one recent study indicated that excess electron/hole could enhance the ductility/strength of some face centered cubic (fcc) metals [47].

## 5. Supplementary material

The supplementary material (SM) includes deformation mechanism of $B_4C$ along (001)[100] slip system under the 2 h-injected state (Fig. S6); deformation mechanism of $B_{13}C_2$ along (001)[100] slip system under the 1 h-injected state (Fig. S7); Fig. S1 indicating the structural evolution of neutral $B_4C$ system shear along (001)[100] slip system; Fig. S2 showing the shear-stress - shear-strain relationship of various $B_4C$ supercell with the same electron concentration and the structural evolution of 4 × 2 × 2 supercell shear along (001)[100] slip system; Fig. S3 displaying the pCOHP analysis for the icosahedral B51-C8 bond under neutral and 1e-injected state; Fig. S4 revealing the shear-stress - shear-strain relationship of various $B_4C$ supercell with the same hole concentration and the structural evolution of 4 × 2 × 2 supercell shear along (001)[100] slip system; and Fig. S5 showing the pCOHP analysis for the icosahedral B51-C8 bond under neutral and 1 h-injected state.

## Declaration of Competing Interest

The authors declare that they have no known competing financial interests or personal relationships that could have appeared to influence the work reported in this paper.

## Acknowledgement

Y.D. Shen and Q.A. were supported by National Science Foundation (CMMI-1727428).

## Appendix A. Supplementary data

Supplementary material related to this article can be found, in the online version, at doi:https://doi.org/10.1016/j.jeurceramsoc.2020.06.004.

## References

[1] V. Domnich, S. Reynaud, R.A. Haber, M. Chhowalla, Boron carbide: structure, properties, and stability under stress, J. Am. Ceram. Soc. 94 (11) (2011) 3605–3628.

[2] F. Thevenot, Boron carbide—a comprehensive review, J. Eur. Ceram. Soc. 6 (4) (1990) 205–225.

[3] A.K. Suri, C. Subramanian, J.K. Sonber, T. Murthy, Synthesis and consolidation of boron carbide: a review, Int. Mater. Rev. 55 (1) (2010) 4–40.

[4] D. Emin, Unusual properties of icosahedral boron-rich solids, J. Solid State Chem. 179 (9) (2006) 2791–2798.

[5] M.M. Balakrishnarajan, P.D. Pancharatna, R. Hoffmann, Structure and bonding in boron carbide: the invincibility of imperfections, New J. Chem. 31 (4) (2007) 473–485.

[6] M. Chen, J.W. McCauley, K.J. Hemker, Shock-induced localized amorphization in boron carbide, Science. 299 (5612) (2003) 1563–1566.

[7] Q. An, W.A. Goddard III, T. Cheng, Atomistic explanation of shear-induced amorphous band formation in boron carbide, Phys. Rev. Lett. 113 (9) (2014) 095501.

[8] Q. An, W.A. Goddard III, Microalloying boron carbide with silicon to achieve dramatically improved ductility, J. Phys. Chem. Lett. 5 (23) (2014) 4169–4174.

[9] Q. An, W.A. Goddard III, Nanotwins soften boron-rich boron carbide ($B_{13}C_2$), Appl. Phys. Lett. 110 (11) (2017) 111902.

[10] Q. An, W.A. Goddard III, K.Y. Xie, G.D. Sim, K.J. Hemker, T. Munhollon, M.F. Toksoy, R.A. Haber, Superstrength through nanotwinning, Nano Lett. 16 (12) (2016) 7573–7579.

[11] Y. Shen, G. Li, Q. An, Enhanced fracture toughness of boron carbide from microalloying and nanotwinning, Scripta Mater. 162 (2019) 306–310.

[12] B. Tang, Q. An, W.A. Goddard III, Improved ductility of boron carbide by microalloying with boron suboxide, J. Phys. Chem. C. 119 (43) (2015) 24649–24656.

[13] B. Tang, Y. He, W.A. Goddard III, Q. An, First principles predicting enhanced ductility of boride carbide through magnesium microalloying, J Am. Ceram. Soc. 102 (9) (2019) 5514–5523.

[14] V. Adasch, M. Schroeder, D. Kotzott, T. Ludwig, N. Vojteer, H. Hillebrecht, Synthesis, crystal structure, and properties of $Mg_xB_{50}C_8$ or $Mg_x(B_{12})_4(CBC)_2(C_2)_2$ ($x = 2.4$-4), J. Am. Chem. Soc. 132 (39) (2010) 13723–13732.

[15] A.U. Khan, A.M. Etzold, X.K. Yang, V. Domnich, K.Y. Xie, C. Hwang, K.D. Behler, M.W. Chen, Q. An, J.C. LaSalvia, K.J. Hemker, W.A. Goddard III, R.A. Haber, Locating Si atoms in Si-doped boron carbide: a route to understand amorphization mitigation mechanism, Acta. Mater. 157 (2018) 106–113.

[16] H. Hillebrecht, N. Vojteer, V. Sagawe, K. Hofmann, B. Albert, Synthesis and characterization of li-containing boron carbide r-$Li_{\sim1}B_{13}C_2$, Z Anorg. Allg. Chem. 645 (3) (2019) 362–369.

[17] Y. He, Y. Shen, B. Tang, Q. An, Strengthening boron carbide through lithium dopant, J. Am. Ceram. Soc. 103 (3) (2020) 2012–2023.

[18] D.Z. Guo, S.X. Song, R.C. Luo, W.A. Goddard III, M.W. Chen, K.M. Reddy, Q. An, Grain boundary sliding and amorphization are responsible for the reverse Hall-petch relation in superhard nanocrystalline boron carbide, Phys. Rev. Lett. 121 (14) (2018) 145504.

[19] X. Yang, S.P. Coleman, J.C. Lasalvia, W.A. Goddard III, Q. An, Shear-induced brittle failure along grain boundaries in boron carbide, ACS Appl. Mater. Interfaces. 10 (5) (2018) 5072–5080.

[20] H. Wang, Q. An, Band-gap engineering in high-temperature boron-rich icosahedral compounds, J. Phys. Chem. C. 123 (19) (2019) 12505–12513.

[21] R.W. Miles, G. Zoppi, I. Forbes, Inorganic photovoltaic cells, Mater Today. 10 (11) (2007) 20–27.

[22] P.P. Altermatt, A. Schenk, F. Geelhaar, G. Heiser, Reassessment of the intrinsic carrier density in crystalline silicon in view of band-gap narrowing, J Appl. Phys. 93

(3) (2003) 1598–1604.

[23] A. Kanevce, M.O. Reese, T. Barnes, S. Jensen, W. Metzger, The roles of carrier concentration and interface, bulk, and grain-boundary recombination for 25% efficient CdTe solar cells, J. Appl. Phys. 121 (21) (2017) 214506.

[24] Y. Oshima, A. Nakamura, K. Matsunaga, Extraordinary plasticity of an inorganic semiconductor in darkness, Science 360 (6390) (2018) 772–774.

[25] H. Wang, S.I. Morozov, W.A. Goddard III, Q. An, Light irradiation induced brittle-to-ductile and ductile-to-brittle transition in inorganic semiconductors, Phys. Rev. B. 99 (16) (2019) 161202.

[26] H. Wang, S. Song, X. Zou, F. Wang, Z. Zhang, S.I. Morozov, X. Wang, K.M. Reddy, Q. An, Photomechanical effect leading to extraordinary ductility in covalent semiconductors, Phys. Rev. B. 100 (9) (2019) 094110.

[27] C. Levade, J.J. Couderc, G. Vanderschaeve, D. Caillard, A. Couret, TEM insitu observation of recombination-enhanced mobility of dislocations in ii-vi compounds, Appl. Surf. Sci. 50 (1–4) (1991) 119–124.

[28] Y. Shen, H. Wang, Q. An, Enhanced ductility of III-v covalent semiconductors from electrons and holes, J. Appl. Phys. 126 (2019) 195105.

[29] J.P. Perdew, K. Burke, M. Ernzerhof, Generalized gradient approximation made simple, Phys. Rev. Lett. 78 (7) (1997) 1396-1396.

[30] G. Kresse, J. Furthmuller, Efficient iterative schemes for ab initio total-energy calculations using a plane-wave basis set, Phys. Rev. B. 54 (16) (1996) 11169–11186.

[31] G. Kresse, J. Furthmuller, Efficiency of ab-initio total energy calculations for metals and semiconductors using a plane-wave basis set, Comp. Mater. Sci. 6 (1) (1996) 15–50.

[32] G. Kresse, J. Hafner, Ab initio molecular dynamics for liquid metals, Phys. Rev. B. 47 (1) (1993) 558–561.

[33] P.E. Blochl, O. Jepsen, O.K. Andersen, Improved tetrahedron method for brillouin-zone integrations, Phys. Rev. B. 49 (23) (1994) 16223–16233.

[34] V. Matkovich, Interstitial compounds of boron, J. Am. Chem. Soc. 83 (8) (1961) 1804–1806.

[35] Y. Le Page, P. Saxe, Symmetry-general least-squares extraction of elastic data for strained materials from ab initio calculations of stress, Phys. Rev. B. 65 (10) (2002) 104104.

[36] R. Hill, The elastic behaviour of a crystalline aggregate, Proc. Phys. Soc. A. 65 (5) (1952) 349–354.

[37] D. Roundy, C.R. Krenn, M.L. Cohen, J.W. Morris, Ideal shear strengths of fcc aluminum and copper, Phys. Rev. Lett. 82 (13) (1999) 2713–2716.

[38] V.L. Deringer, A.L. Tchougréeff, R. Dronskowski, Crystal orbital hamilton population (COHP) analysis as projected from plane-wave basis sets, J. Phy. Chem. A. 115 (21) (2011) 5461–5466.

[39] S. Maintz, V.L. Deringer, A.L. Tchougréeff, R. Dronskowski, LOBSTER: a tool to extract chemical bonding from plane-wave based DFT, J. Comput. Chem. 37 (11) (2016) 1030–1035.

[40] S. Steinberg, R. Dronskowski, The crystal orbital Hamilton population (COHP) method as a tool to visualize and analyze chemical bonding in intermetallic compounds, Crystals 8 (5) (2018) 225.

[41] K. Momma, F. Izumi, VESTA 3 for three-dimensional visualization of crystal, volumetric and morphology data, J. Appl. Crystallogr. 44 (6) (2011) 1272–1276.

[42] M. Liu, C. Liu, U.P. Kumar, M. Chen, Exploring configurations and properties of boron carbide by first principle, Mater. Res. Express. 7 (1) (2020) 015904.

[43] K. Wade, The structural significance of the number of skeletal bonding electron-pairs in carboranes, the higher boranes and borane anions, and various transition-metal carbonyl cluster compounds, J. Chem. Soc. D. (15) (1971) 792–793.

[44] D. Mingos, A general theory for cluster and ring compounds of the main group and transition elements, Nature Phys. Sci. 236 (68) (1972) 99–102.

[45] S.F. Pugh, Relations between the elastic moduli and the plastic properties of polycrystalline pure metals, Philos. Mag. 45 (367) (1954) 823–843.

[46] K.M. Reddy, P. Liu, A. Hirata, T. Fujita, M.W. Chen, Atomic structure of amorphous shear bands in boron carbide, Nat. Commun. 4 (1) (2013) 2483.

[47] H. Wang, J. Fuller, P. Chen, S.I. Morozov, Q. An, Characterizing local metallic bonding variation induced by external perturbation, Phys. Chem. Chem. Phys. 22 (4) (2020) 2372–2378.